Hindawi
Advances in Civil Engineering
Volume 2022, Article ID 7771358, 21 pages
https://doi.org/10.1155/2022/7771358

Research Article

The Influence of Wind Shielding and Train-Induced Wind on the Vibration of a Train-Bridge System

Yujing Wang,[1] **Xuexiang Xv**,[2] **Shanshan Wang**,[3] **and Qinghai Guan**[1]

[1]*School of Traffic Engineering, Shandong Jianzhu University, Jinan 250101, China*
[2]*China Communications Construction Company Limited, Beijing 10088, China*
[3]*Shandong Hi-Speed Group Co., Ltd., Jinan 250098, China*

Correspondence should be addressed to Yujing Wang; qearjing@163.com

Received 20 April 2022; Revised 25 August 2022; Accepted 17 September 2022; Published 15 October 2022

Academic Editor: Cristoforo Demartino

The aerodynamic forces of the system were obtained based on a 3D aerodynamic model, and a dynamic analysis model of the train-bridge coupling system was established to compare the vibration responses of the train and bridge with and without a wind barrier to fully consider the wind shielding effect and train-induced wind effect on the vibration of a train-bridge system. The results show that the combined wind direction and the direction of the operating train are at an angle. Although the shape of the leading and trailing cars is the same, their wind load values are not the same due to the influence of the train wind. Because of the perforations, the vortex between the wind barrier and the train's windward surface varies in a complicated fashion. The airflow traveling through the holes has a negative value because it circulates at the intersection of the windward surface and the top surface of the car body. The vehicles' lateral wheel force, derailment factor, offload factor, and overturning factor are all lowered when the wind barrier is erected. The shielding effect of the wind barrier on the head car is more noticeable when it comes to lateral wheel force and derailment factor. With a wind barrier installed, the wind field surrounding the bridge is very complex, resulting in a modest decrease in vertical displacement.

1. Introduction

The number of railways constructed in gorges, deserts, straits, and other windy locations is growing in tandem with the fast building of China's HSR (high-speed railway) networks. Crosswinds are the principal factor limiting train speed and impacting the train's operating safety in windy areas [1]. The most common measures used to ensure the safe operation of trains are the installation of a wind shielding wall on embankment lines and wind barriers on bridge lines. Many researchers prefer the gap-type wind barrier among them [2–5]. It not only decreases the weight of the bridge but also provides a reduced wind velocity safety zone for trains. At the same time, the train-induced wind field created by the train's high-speed movement cannot be disregarded as it accelerates. The combined wind field synthesized by the train-induced wind field and the crosswind field in a crosswind environment is exceedingly intricate [6].

Many researchers throughout the globe have conducted substantial study on the wind shielding effect and parameter optimization of wind barriers during the last two decades. Hui et al. [7] suggested a louvered wind barrier and used a scale wind tunnel test to further improve the louvered wind barrier's specifications. Xiong et al. [8] investigated the noise barrier's transient aerodynamic pressure, which was created by two distinct full-size trains passing by at speeds ranging from 380 to 420 km/h. By modeling the aerodynamic performance of the maglev train passing through the noise barriers, Luo et al. [9] investigated the influence of the sound barrier on the flow field surrounding it. Gu et al. [10] investigated how the flow field structure changes when various kinds of wind barriers are used, as well as how effective they are at sheltering trains on railway bridges. Buljac et al. [11] investigated the impact of wind barriers on the flow characteristics surrounding the bridge deck using the

wind tunnel test technique. Deng et al. [12] investigated the effect of a wind barrier of a given height and porosity on the flow field structure and train operating safety.

Numerical simulation approaches have also been used to study the train-induced wind effect [13]. Huang et al. [14], for example, employed the IDDES approach to study train-induced wind and slipstream characteristics around a CRH2 high-speed train. With the use of large-eddy simulation (LES), Hassan et al. [15] evaluated the slipstream and wake flow of a simplified five-coach ICE2-shaped train (LES). The greatest train wind speed emerges in the streamlined head and in the train's wake region, according to some conclusions. For researching wind fields and wind loads, wind tunnel testing is also a suitable option. Dorigatti et al. [16] analyzed the three-component force and pressure coefficient of the motor vehicle model and the stationary car model under crosswind using CFD and wind tunnel experiments. However, the motor train model's experimental speed is only 20.8 m/s, which is well below the real speed. The moving train model has also been used to evaluate wind loads by certain researchers. Xiang et al. [17], for example, investigated the force acting on a moving train exposed to crosswinds. The train's speed in the simulation, however, fluctuated from 0.5 to 10 m/s, which is slower than the real train speed.

Existing research on the dynamic response of the train-bridge coupling system does not always take into account the effects of train-induced wind [18–20]. The static three-component force coefficient and the associated wind velocity are thought to be able to calculate the train and bridge's wind load. This calculation technique overestimates the train-bridge system's dynamic reactions, since it fails to discriminate between the loads operating on the train's head, middle, and tail cars, as well as the train's longitudinal aerodynamic force. Furthermore, when a wind barrier is built on the bridge's windward or leeward side, the wind shielding effect of the wind barrier will impact the train's operating safety as well as the bridge's dynamic reactions. Only a few researchers have looked at the impact of the windbreak and train-induced wind on the system's vibrational properties. The authors of this research looked at the wind load on the vehicle and bridge in a combined wind field and assessed how varied train speeds and wind velocities affected them.

This work employs a novel overset mesh approach to compute the aerodynamic forces of the system incorporating the train-induced wind impact, based on the technical background of a HSR line in a windy environment. Then, using MATLAB software to construct the calculation analysis program and perform the vehicle-bridge system vibration analysis, a wind-train-bridge coupling system dynamic calculation model is created. A technique for vibration analysis of a train-bridge system (with installed wind barrier) that takes into account both the windbreak effect and the train-induced wind effect is developed, and a case study is analyzed.

2. Engineering Background and CFD Model

2.1. Engineering Background. The Chinese second Lanzhou–Xinjiang double-line railway (also known as the second Lan–Xin railway) extends from Lanzhou Station in Gansu Province to Urumqi in the west, passing through five windy areas. The line's overall length is 1776 kilometers, with the line in the windy region accounting for around 32.6% of the whole length. Furthermore, the railway design's maximum speed is 250 km/h, which is much faster than the current Lan–Xin railway. As a result, while operating in a windy location, high-speed trains have a constant risk of flipping, which is very hazardous [21]. In this study, a 10-span simply supported box girder bridge situated in a typical windy environment is chosen as the research object for analysis.

2.2. Governing Equations. The equations governing the flow around the train-bridge system are the continuum and momentum equations, which take the following tensor forms:

The continuum equation is as follows:

$$\operatorname{div}\vec{u} = 0. \tag{1}$$

The momentum equation is as follows:

$$\begin{cases} \operatorname{div}(u\vec{u}) = -\dfrac{1}{\rho}\dfrac{\partial p}{\partial x} + v\operatorname{div}(\operatorname{grad} u), \\ \operatorname{div}(v\vec{u}) = -\dfrac{1}{\rho}\dfrac{\partial p}{\partial y} + v\operatorname{div}(\operatorname{grad} v), \\ \operatorname{div}(w\vec{u}) = -\dfrac{1}{\rho}\dfrac{\partial p}{\partial z} + v\operatorname{div}(\operatorname{grad} w), \end{cases} \tag{2}$$

where $\vec{u}$ is the velocity in the coordinate system; u, v, and w are the speed components in x, y, and z directions, respectively; ρ is the density; p is the air pressure of the fluid; and v is the kinetic viscosity of the air.

The RNG k-ε model is as follows:

$$\begin{aligned} \frac{\partial(\rho k)}{\partial t} + \frac{\partial(\rho k u_i)}{\partial x_i} &= \frac{\partial}{\partial x_j}\left[(\alpha_k \mu_{\text{eff}})\frac{\partial k}{\partial x_j}\right] + G_k + \rho\varepsilon, \\ \frac{\partial(\rho\varepsilon)}{\partial t} + \frac{\partial(\rho\varepsilon u_i)}{\partial x_i} &= \frac{\partial}{\partial x_j}\left[(\alpha_\varepsilon \mu_{\text{eff}})\frac{\partial \varepsilon}{\partial x_j}\right] + C_{1\varepsilon}^{*}\frac{\varepsilon}{k}G_{\text{k}} - C_{2\varepsilon}\rho\frac{\varepsilon^2}{k}, \end{aligned} \tag{3}$$

where $G_k = \mu_t(\partial u_i/\partial x_j + \partial u_j/\partial x_i)\partial u_i/\partial x_j$; $\mu_{\text{eff}} = \mu + \mu_t$, $\mu_t = \rho C_\mu k^2/\varepsilon$, $C_\mu = 0.0845$; α_k and α_ε are the reciprocal of the turbulent Prandtl number for the turbulent kinetic energy k and dissipation rate ε, respectively, $\alpha_k = \alpha_\varepsilon = 1.39$; $C_{1\varepsilon}^{*} = C_{1\varepsilon} - \eta(1 - \eta/\eta_0)/1 + \beta\eta^3, \eta = \sqrt{2E_{ij}\cdot E_{ij}}k/\varepsilon$, $E_{ij} = 1/2(\partial u_i/\partial x_j + \partial u_j/\partial x_i)$, $\eta_0 = 4.38$, $\beta = 0.012$; $C_{1\varepsilon} = 1.42$, and $C_{2\varepsilon} = 1.68$.

The equation to calculate y^+ is as follows:

$$y^+ = \frac{\Delta y \rho u_\tau}{\mu} = \frac{\Delta y}{\nu}\sqrt{\frac{\tau_w}{\rho}}, \quad (4)$$

where u is the hourly average velocity of the fluid; u_τ is the wall friction velocity, $u_\tau = \sqrt{\tau_w/\rho}$, in which τ_w is the wall shear stress; and Δy is the distance to the wall.

2.3. Aerodynamic Model. Windshield height, porosity, opening shape, installation location, and other parameters all have an impact on windshield efficiency. According to certain academic study, a wind barrier with a specified parameter was chosen for numerical simulation (height $H = 3.0$ m; porosity $\beta = 30\%$) [22]. To prevent the scale effect, the scale ratio was set to 1 : 1 while creating the wind barrier-train-bridge CFD aerodynamic model, as shown in Figure 1. The train model chosen is a three-car CRH2 high-speed train. Because the middle cars' lengths are the same, several of the vehicles in the middle are simplified, leaving just the head cars, tail cars, and one middle car. The high-speed operation of the train is simulated, and the characteristics of the wind field under crosswinds are examined, using the fluid mechanics program STAR-CCM+. Because the holes in the wind barrier are circular and tiny, the mesh must be encrypted near them.

Because the train is traveling at such a high speed, the flow field is calculated as a three-dimensional incompressible turbulent flow that is erratic. As a result, in a second-order upwind style, the RNG k-ε turbulence model is employed to discretize the convection term. The SIMPLE technique is a popular approach for pressure adjustment. This approach is used to compute the pressure field initially in this study. After solving the discrete momentum equations, a velocity field is obtained, which is then utilized to change the pressure equation. An iterative approach is used to adjust the pressure in this manner. The boundary conditions include velocity-inlet for inlet, pressure-outlet for outlet, and nonslip wall for the surface of train and bridge. The wall function approach is used in the near-wall region, with the boundary layers of the railway wall and bridge surface set to 8 layers and a total of 23.24 million grids. The length, breadth, and height of the calculation domain are 300, 75, and 220 meters, respectively. Set the velocity-inlet to the inlet of the incoming flow surface, the pressure-outlet to the outlet surface, the other boundaries to wall surfaces, and the vehicle body and bridge surfaces to frictional wall surfaces.

Figure 2 shows the geometry of the vehicle and bridge models. The headstock is a complicated three-dimensional curved surface with a length of 9.5 m. The car body is 3.38 m in width and 3.7 m in height. The length of the head car and the tail car is 25.7 m, and that of the middle car is 25 m, so the total length of the train model is 76.4 m. The bridge model is simplified as a 300 m long continuous beam with a solid section, without considering the piers. The profile of the beam is retained as its original shape, whose height and width are, respectively, 2.85 m and 12.2 m. The height, thickness, and length of the wind barrier are 3.5 m, 0.3 m, and 300 m, respectively.

To simulate train movement, the moving grid technique, sliding grid method, and overset grid approach are being employed. The overset grid approach is employed in this research to replicate the train's absolute velocity, as seen in Figure 3. Overset meshes are also known as Chimera meshes or overlapping meshes. The essential notion is that the fluid calculational area is divided into numerous relatively simple subregions, each of which creates meshes separately. The flow field information is sent by interpolation in the overlapping, nesting, or covering border areas, and the subregions have overlapping, nesting, or covering interactions with each other. The complexity of grid production is decreased and the quality of the first grid is ensured by splitting the calculational domain. As a result, overset meshes are often utilized to solve the issue of several objects moving relative to each other in the flow field. Mesh refinement was done around wind barriers, cars, and bridges to increase calculational accuracy. The length of the bridge and the calculational domain are both 300 meters in the developed model. To increase calculation performance and ensure result correctness, the time step of the train movement throughout the calculation is adjusted to 0.001 s after repeated and iterative calculations and comparisons.

2.4. Validation of the CFD Numerical Model. The accuracy of numerical simulation results is often influenced by turbulence models and grids. For CFD numerical calculations, the aerodynamic model from Section 2.3 is employed. The wind velocity U in the numerical simulation and the wind tunnel test is the same, being 10 m/s, to prevent the effect of the difference in wind velocity on the findings. Because the train model in the test is a static vehicle model, the CFD numerical simulation uses the same car model. A comparison of test and CFD simulation results is shown in Table 1.

In Table 1, C_D, C_L, and C_M are three-component force coefficients. As can be seen from Table 1, the numerical error of C_D and C_L of vehicles and bridges obtained by simulation and test is within 20%, which shows that the meshing method and turbulence model used in CFD simulation are reasonable. Vehicles and bridges have quite significant moment coefficients. This is due to the fact that the moment coefficient is tiny, which makes it difficult to acquire precise simulation values, resulting in huge calculation errors.

3. Wind-Train-Bridge Coupled Vibration Analysis Method

3.1. System Motion Equation. The wind is regarded as a stable and random process associated with space as an integral aspect of the wind-vehicle-bridge system [23]. A 22-degree-of-freedom vehicle model (containing 6 for the car body, 6 for the bogie, and 1 for the wheelset) is constructed to examine the train's aerodynamic forces in motion. Figure 4 depicts the car's model.

Figure 5 shows a finite element model of a 10-span simply supported beam created using the commercial finite element program Ansys, where the x direction is the train's

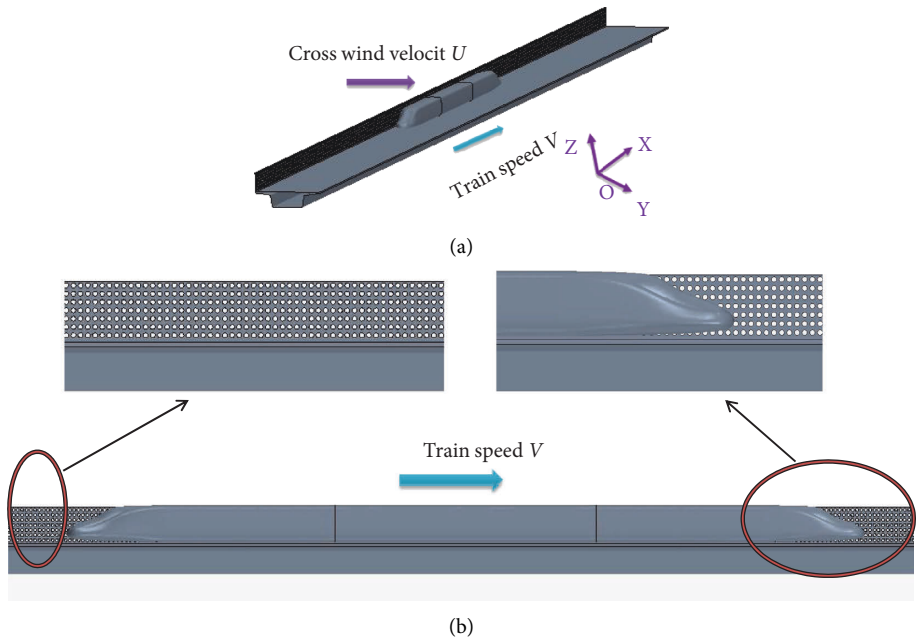

Figure 1: Geometric model composed of wind barriers, cars, and bridges.

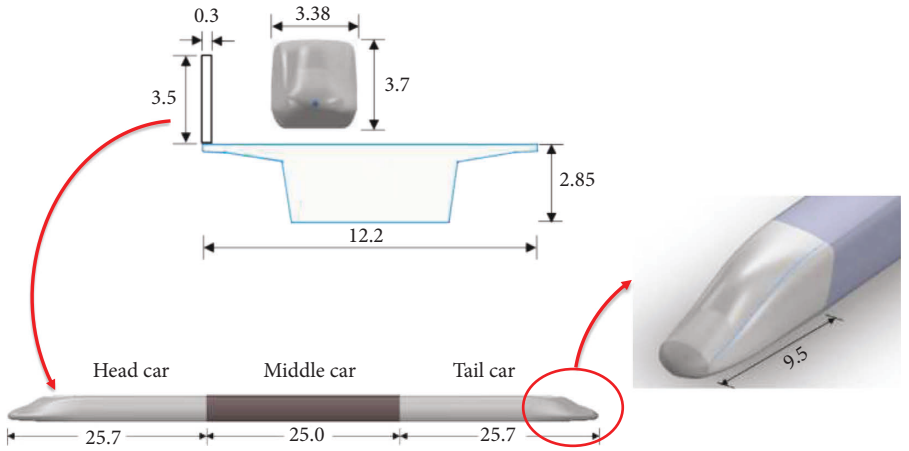

Figure 2: Dimensions of vehicle models and bridge models (unit: m).

moving direction, the z direction is vertically upward, and the y direction is the crosswind's intake direction. The components of beam 188 are used to construct beams and piers in the model, which both have a variable cross section. The beam length is 327.8 meters, and the pier height is 20 meters. The length of the expansion joints between each bridge span is 0.2 m, as per the building specifications. To calculate the dynamic response of the bridge in MATLAB software, the direct stiffness method is used to extract the mass matrix $\mathbf{M}_b$ and stiffness matrix $\mathbf{K}_b$ of the bridge finite element model, and the data format is processed in MATLAB. The damping matrix $\mathbf{C}_b$ was calculated by the Rayleigh method, namely, $\mathbf{C}_b = \alpha \bullet M_b + \beta \bullet K_b$.

$$\begin{bmatrix} \mathbf{M}_{vv} & 0 \\ 0 & \mathbf{M}_{bb} \end{bmatrix} \left\{ \ddot{\mathbf{X}}_v \ddot{\mathbf{X}}_b \right\} + \begin{bmatrix} \mathbf{C}_{vv} & \mathbf{C}_{vb} \\ \mathbf{C}_{bv} & \mathbf{C}_{bb} \end{bmatrix} \begin{Bmatrix} \dot{\mathbf{X}}_v \\ \dot{\mathbf{X}}_b \end{Bmatrix} + \begin{bmatrix} \mathbf{K}_{vv} & \mathbf{K}_{vb} \\ \mathbf{K}_{bv} & \mathbf{K}_{bb} \end{bmatrix} \begin{Bmatrix} \mathbf{X}_v \\ \mathbf{X}_b \end{Bmatrix} = \begin{Bmatrix} \mathbf{F}_{vb} \\ \mathbf{F}_{bv} \end{Bmatrix} + \begin{Bmatrix} \mathbf{F}_{vw} \\ \mathbf{F}_{bw} \end{Bmatrix}, \tag{5}$$

where $\mathbf{M}$, $\mathbf{C}$, and $\mathbf{K}$ are the mass, damping, and stiffness matrices; $\ddot{\mathbf{X}}$, $\dot{\mathbf{X}}$, and $\mathbf{X}$ are the acceleration, velocity, and displacement vectors, respectively; the subscripts b and v represent the bridge and the vehicle, respectively; $\mathbf{F}_{vb}$ and $\mathbf{F}_{bv}$ are the same in magnitude and are the interaction force between the vehicle and the bridge; and $\mathbf{F}_{vw}$ and $\mathbf{F}_{bw}$ are both wind load.

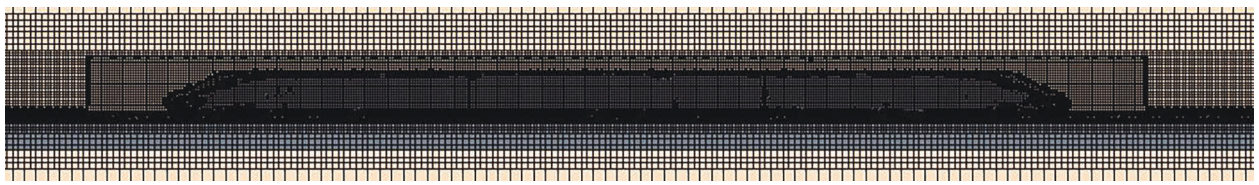

(a)

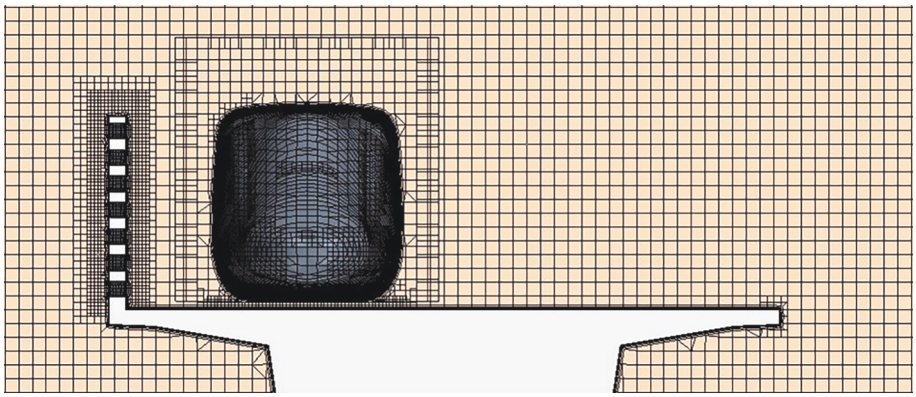

(b)

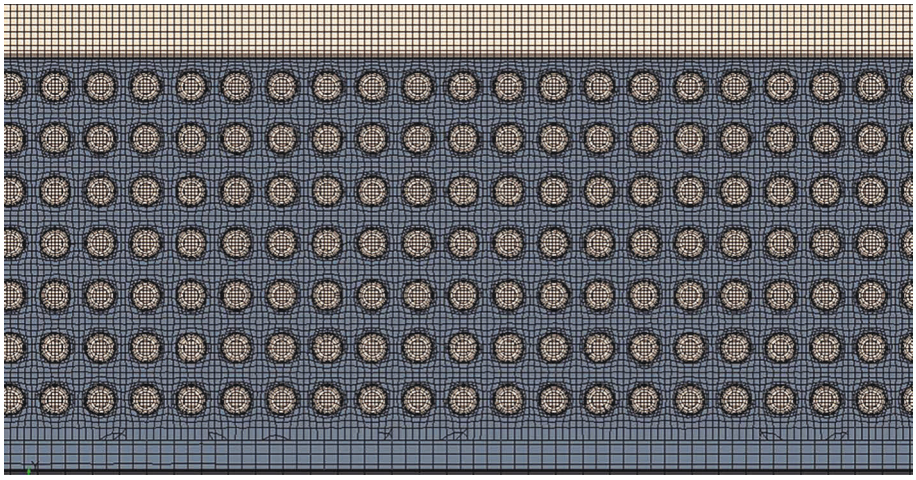

(c)

Figure 3: Meshes of the model. (a) Overset mesh around the train. (b) Cross section mesh. (c) Mesh around the barrier.

Table 1: Comparison of results from tests and CFD simulation.

Model		C_D	C_L	C_M
Train	Test	0.38	0.33	0.04
	Simulation	0.34	0.28	−0.02
Bridge	Test	2.70	0.10	0.07
	Simulation	2.45	0.12	0.11

3.2. Wind Loads. The calculation settings are specified for numerical simulation to immediately derive the wind load in the combined wind field from the numerical model (wind velocity $U = 20$ m/s; train speed $V = 200$ km/h). The train's static wind load is shown in Table 2 as the force acting on three cars. There is no resistance component in the bridge model's wind load, which is the value per unit length of the bridge. The train produces an angle with the

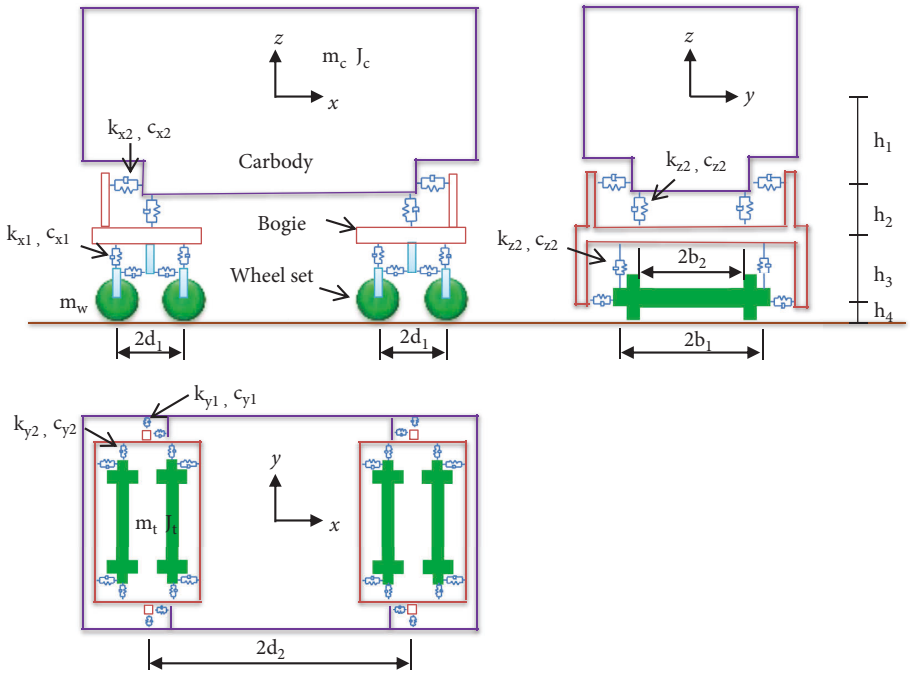

Figure 4: Vehicle model.

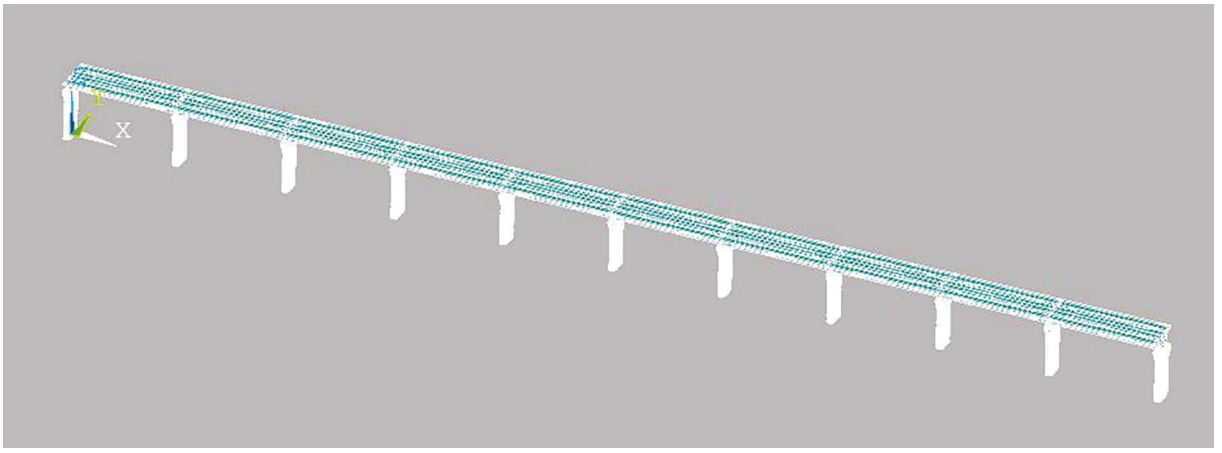

Figure 5: Bridge model.

Table 2: Wind loads of the train and wind loads of the bridge per unit length.

Model		Resistance (N)	Drag force (N)	Lift (N)	Moment (N·m)
Train	Head car	1699.20	14205.59	2827.35	−4336.22
	Middle car	−1322.75	3824.56	2394.35	−1589.80
	Tail car	−6241.06	−6345.59	899.84	−211.10
Bridge		—	2690.99	3908.66	10703.05

Note. The symbol — indicates that the value does not exist.

combined wind field generated by the superposition of the crosswind perpendicular to the bridge and the train-induced wind along the train's running path. The weights on the head and tail cars are extremely similar, despite the fact that their shapes are almost identical. However, owing to the impact of train-induced wind, the wind load values are not precisely the same.

The buffeting force, like static wind, has a serious impact on the vibration response of the vehicle. Its calculation is shown in the following formula [24]:

$$F_{\mathrm{D}}^{\mathrm{bf}} = \frac{1}{2}\rho A\overline{V}_{\mathrm{R}}^{2}\left[C_{\mathrm{F_S}}(\varphi)\cdot\frac{2\overline{u}u}{\overline{V}_{\mathrm{R}}^{2}} + C'_{\mathrm{F_S}}(\varphi)\cdot\frac{w}{\overline{U}}\right],$$

$$F_{\mathrm{L}}^{\mathrm{bf}} = \frac{1}{2}\rho A\overline{V}_{\mathrm{R}}^{2}\left[C_{\mathrm{F_L}}(\varphi)\cdot\frac{2\overline{u}u}{\overline{V}_{\mathrm{R}}^{2}} + C'_{\mathrm{F_L}}(\varphi)\cdot\frac{w}{\overline{U}}\right], \quad (6)$$

$$M^{\mathrm{bf}} = \frac{1}{2}\rho A\overline{V}_{\mathrm{R}}^{2}H\left[C_{\mathrm{M}}(\varphi)\cdot\frac{2\overline{u}u}{\overline{V}_{\mathrm{R}}^{2}} + C'_{\mathrm{M}}(\varphi)\cdot\frac{w}{\overline{U}}\right],$$

where F_D^{bf}, F_L^{bf}, an d M^{bf} are the buffeting forces in the lateral, vertical, and torsional directions, respectively; A is the windward area, and ρ is the air density; $\overline{V}_R$ denotes the relative velocity between the train and wind; $C_{F_S}(\varphi), C_{F_L}(\varphi)$, and $C_M(\varphi)$ are static coefficients, and the superscript $'$ refers to the first derivative of them; u and ω stand for the horizontal and vertical fluctuating wind velocity; and φ is the wind attack angle, which is taken to be zero in the calculation.

3.3. Solution of the System. The German low interference spectrum is used to mimic track problems. External stimulation mainly includes track irregularities and wind loads, and the latter are shown in Table 2. The vehicle motion equation is constructed in MATLAB software using the rigid body dynamics approach. To produce the damping matrix, the mass and stiffness matrices are retrieved simultaneously from the Ansys model of the bridge. The MCK matrix of the bridge is repeatedly called during calculation in MATLAB. The vehicle equation and bridge equation are successively solved to produce the dynamic response using the intersystem interaction approach [25], and the calculation process is depicted in Figure 6. The CRH2 train is made up of 2 (MTMTTMTM), a total of 16 cars, and the bridge model consists of 10-span simply supported beams while solving the train-bridge coupled vibration equation.

3.4. Driving Safety Evaluation Index. Track irregularities stimulate high-speed trains as they run along the track. Accidents such as derailment or overturning may occur as a result of unfavorable factors such as wind load, seismic load, and impact. Wheel-rail lateral force, derailment factor, and offload factor are often utilized as assessment indicators for driving safety in the investigation of vehicle-axle coupling vibration. When assessing the influence of wind load, the vehicle's overturning factor should also be taken into account.

3.4.1. Lateral Wheel Force. Trains tend to generate large lateral forces on the rails when running on the bridge due to track irregularities, serpentine waves, or crosswinds, which will not only cause the rails and sleepers to slide laterally or even overturn the rails, but also cause vehicle derailment; therefore, the wheel-rail lateral force must be controlled. The wheelset's lateral horizontal force must fulfill the following requirement:

$$Q \le 10 + \frac{P}{3}, \quad (7)$$

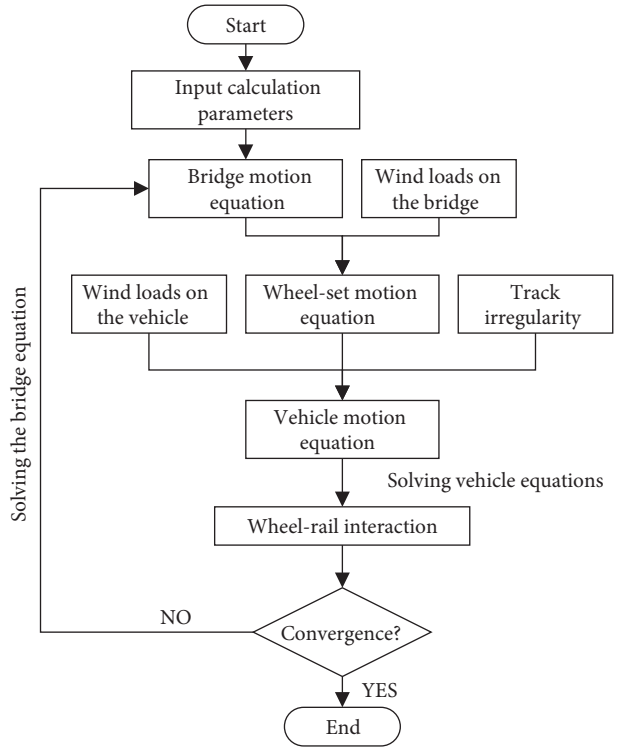

Figure 6: Flowchart of intersystem interaction.

where Q is the wheel-rail lateral force (kN) and P is the static wheel weight (kN).

3.4.2. Derailment Factor. The derailment factor of the train is defined as Q/P, which is an index used to evaluate the derailment stability of the train wheels. The evaluation standard of the derailment factor of the train is as follows:

$$\frac{Q}{P} \le 0.8. \quad (8)$$

3.4.3. Offload Factor. Another essential metric for assessing train operating safety is the wheel load reduction ratio. It mostly discusses the derailment produced by a lateral force increase. The lateral and vertical forces are the primary calculating parameters. The offload factor's safety assessment criterion is as follows:

$$\Delta\frac{P}{P} \le 0.6, \quad (9)$$

where ΔP is the weight of the moving wheel (kN).

3.4.4. Overturning Factor. Under the combined action of different adverse loads, particularly under the action of a strong crosswind, the vehicle is more likely to overturn to the leeward side; hence, the overturning factor D is used to quantify the vehicle's overturning stability. This is how it is defined:

$$D = \frac{P_2 - P_1}{P_2 + P_1} < 0.8 \text{ or } D = \frac{P_d}{P_{st}} < 0.8, \quad (10)$$

where P_1 and P_2 are the vertical forces on the inner and outer wheels, respectively, and the inner side is the possible overturning direction of the relative vehicle body; P_{st} is the vertical static load between the wheel and rail when there is no lateral force; and P_d is the vertical force change between the wheel and rail when there is a lateral force.

The axle loads of the CRH2 motor train and trailer used in this calculation are 135 kN and 120 kN, respectively, according to relevant regulations, and the lateral wheel force limits are 55 kN and 50 kN, respectively.

3.5. Driving Stability Evaluation Index. Vehicle running stability is an essential technical index for measuring a vehicle's running performance, and it is often used to describe the vehicle's vibration performance. The basic foundation for judging passenger comfort is passenger car stability, which represents the influence of vehicle vibration on passenger comfort. The vehicle body acceleration and Sperling index are included in the stability assessment index. Sperling index, which is a comprehensive indicator representing passenger fatigue, is primarily used to assess vehicle stability.

It is specified that the Sperling comfort index is calculated as follows for measuring the vehicle's ride comfort:

$$W = 0.896^{10}\sqrt{a^3/f \cdot F(f)}, \tag{11}$$

where a is the maximum vibration acceleration (m/s^2), f is the vibration frequency (Hz), and $F(f)$ is the frequency correction coefficient.

Vehicle vibration's acceleration and frequency change over time due to its randomness. As a result, in order to calculate the vehicle stationarity index, split the studied acceleration waveform into several groups based on frequency, then calculate the stationarity index of each group, and lastly calculate the vehicle stationarity index using the following formula:

$$W = \sqrt[10]{W_1^{10} + W_2^{10} + \cdots + W_N^{10}}, \tag{12}$$

where W_i is the stationarity index of each frequency grouping and N is the total number of groupings in the whole band. According to relevant regulations, the limits of lateral Sperling and vertical Sperling are both 2.5.

4. Case Study

4.1. Flow Field Analysis. Trains will be able to operate in a safe environment thanks to the wind barrier. The train-bridge system with a/no wind barrier in Section 2.2 is used as the object to assess the flow field of the bridge in order to study its influence on the head, middle, and tail cars on the bridge.

Illustrated in Figure 7 is the pressure distribution of different sections along the z direction:

(1) When the incoming flow is close to the wind barrier-train-bridge system, it acts first on the wind barrier's nonporous position, generating a higher positive pressure. The closer you are to the wind barrier, the greater the pressure. This is because the incoming flow acts vertically on the wind barrier, and the wind velocity reduces immediately, causing the pressure to rise abruptly. A portion of the incoming flow goes through the perforations and acts directly on the train's surface. When there is no wind barrier, the incoming flow acts directly on the vehicle body's windward side, causing a greater pressure on this side.

(2) Although it is obvious that the pressure value on the left side of the body is still positive, the value is reduced dramatically. Because of the existence of holes, the vortex between the wind barrier and the train's windward surface varies in a highly intricate way. The airflow passing through the hole has a negative value and circulates in the upper left corner of the car body. The fluid creates a vortex on the opposite side of the vehicle body after crossing over the train, with the center being negative pressure, and continues to fall away from the car body. There is a vortex even when there is no wind barrier, but the negative pressure value at the center of the vortex is lower than when there is one.

(3) The leeward side causes backflow and forms a vortex as a result of the friction of the wall boundary layer and the energy dissipation caused by the fluid viscosity. At the same time, the train's movement causes the surrounding fluid to move simultaneously, resulting in train-induced wind, which is superimposed on the crosswind to modify the train-bridge system's flow field distribution along the longitudinal bridge direction. The vortex on the leeward side develops and expands longitudinally as a result, generating a complicated wake at the train's rear. When there is no wind barrier, the lowest negative pressure value is found mostly at the intersection of the automobile body's windward side and the roof.

The surface streamline full of pressure, as depicted in Figure 8, is responsible for the flow of the vehicle surface with or without a wind barrier. The flow lines on the vehicle body start to diverge from the head car's nose and bypass the car body to the tail car's rear, as shown in the image. The airflow blows over the head of the train, splits from the windward side and the corner of the roof, and then deflects down the train axis due to the combined effect of crosswind and train-induced wind. This demonstrates the three-dimensionality of the flow characteristics surrounding the train. The wind speed of the crosswind is lowered when the wind barrier is built owing to its blocking impact on the crosswind, lowering the yaw angle. Furthermore, the maximum pressure in the nose area is around 24.6% lower than it would be without the wind barrier. As a result, the pressure on the vehicle's windward side is lessened, and the separation angle at the train's top is lowered. From this, it can be deduced that a higher crosswind wind velocity would result in a bigger yaw angle, resulting in more airflow separation.

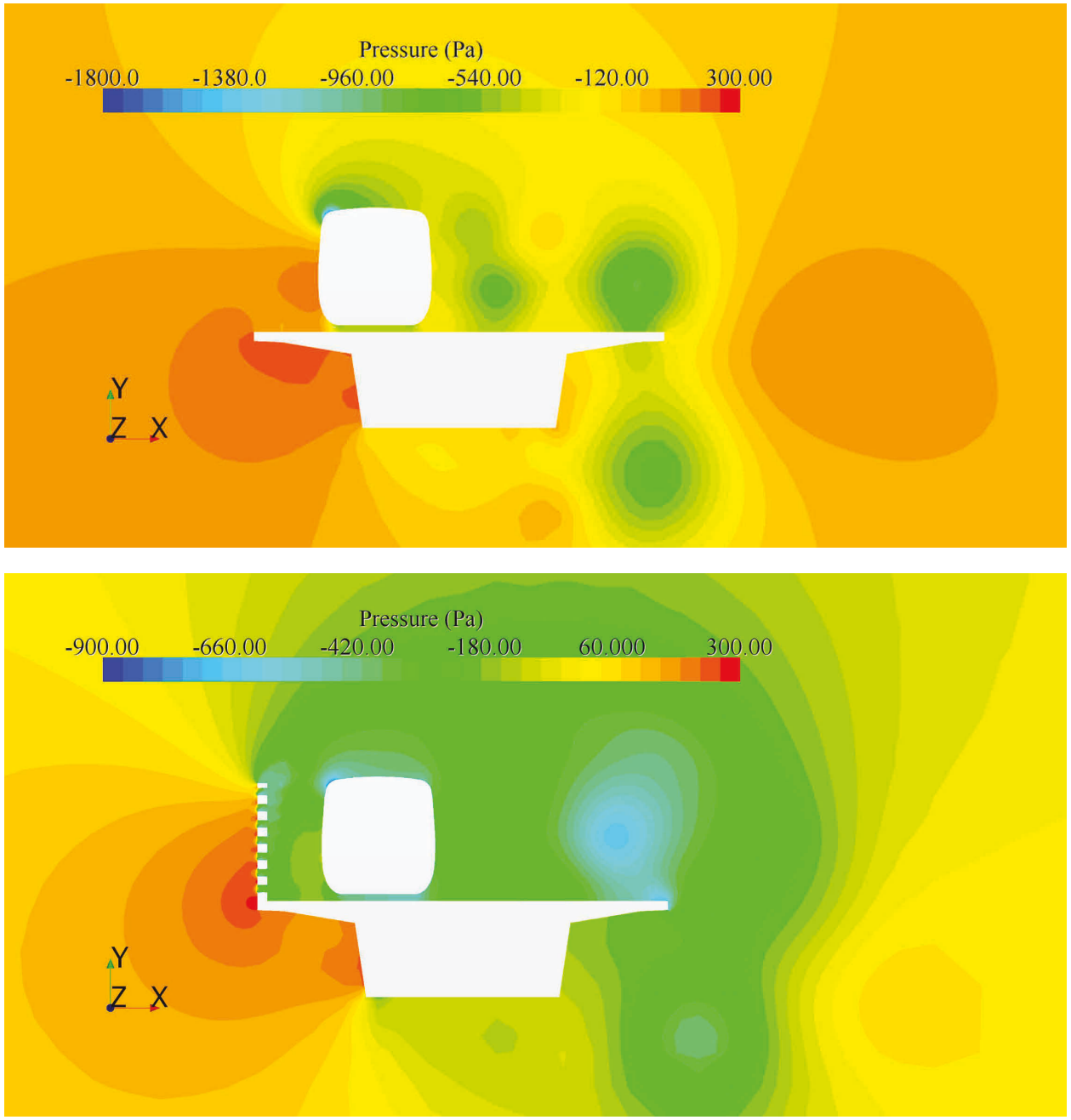

(a)

Figure 7: Continued.

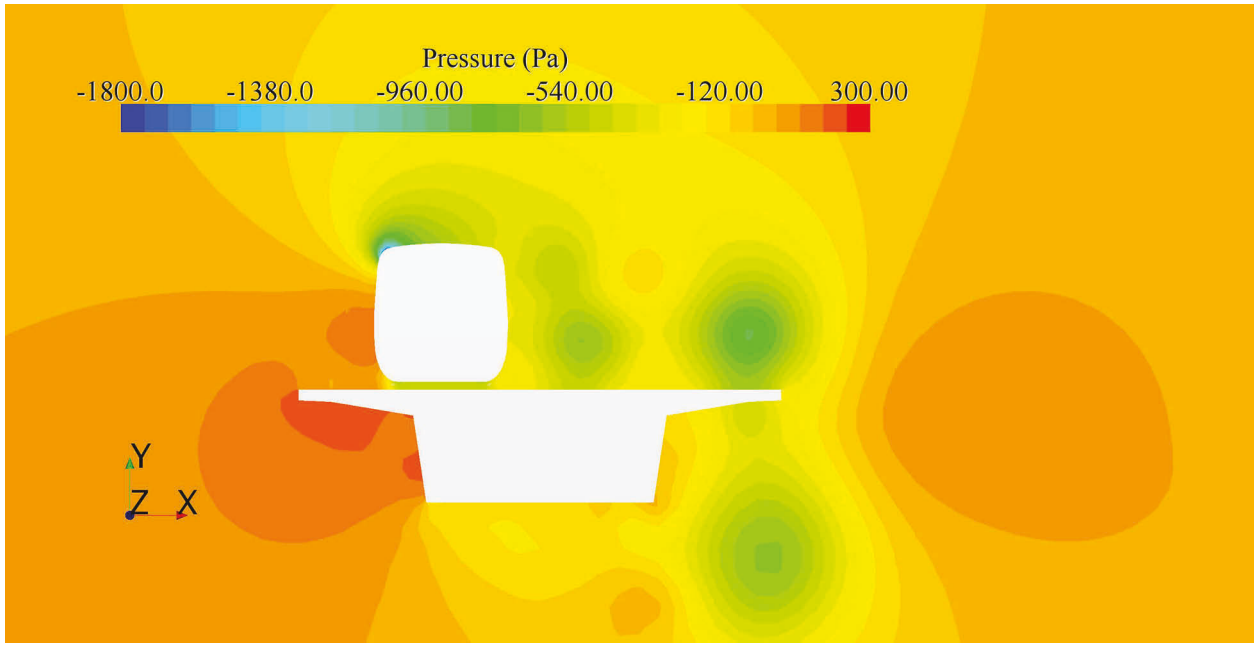

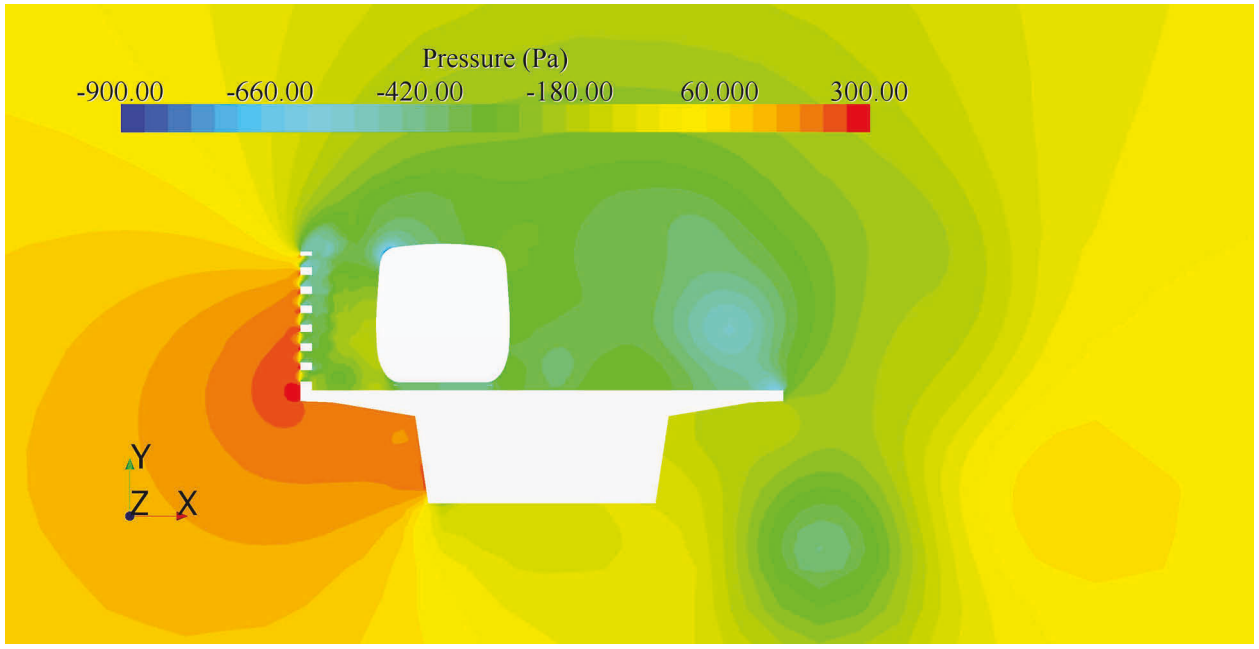

(b)

Figure 7: Continued.

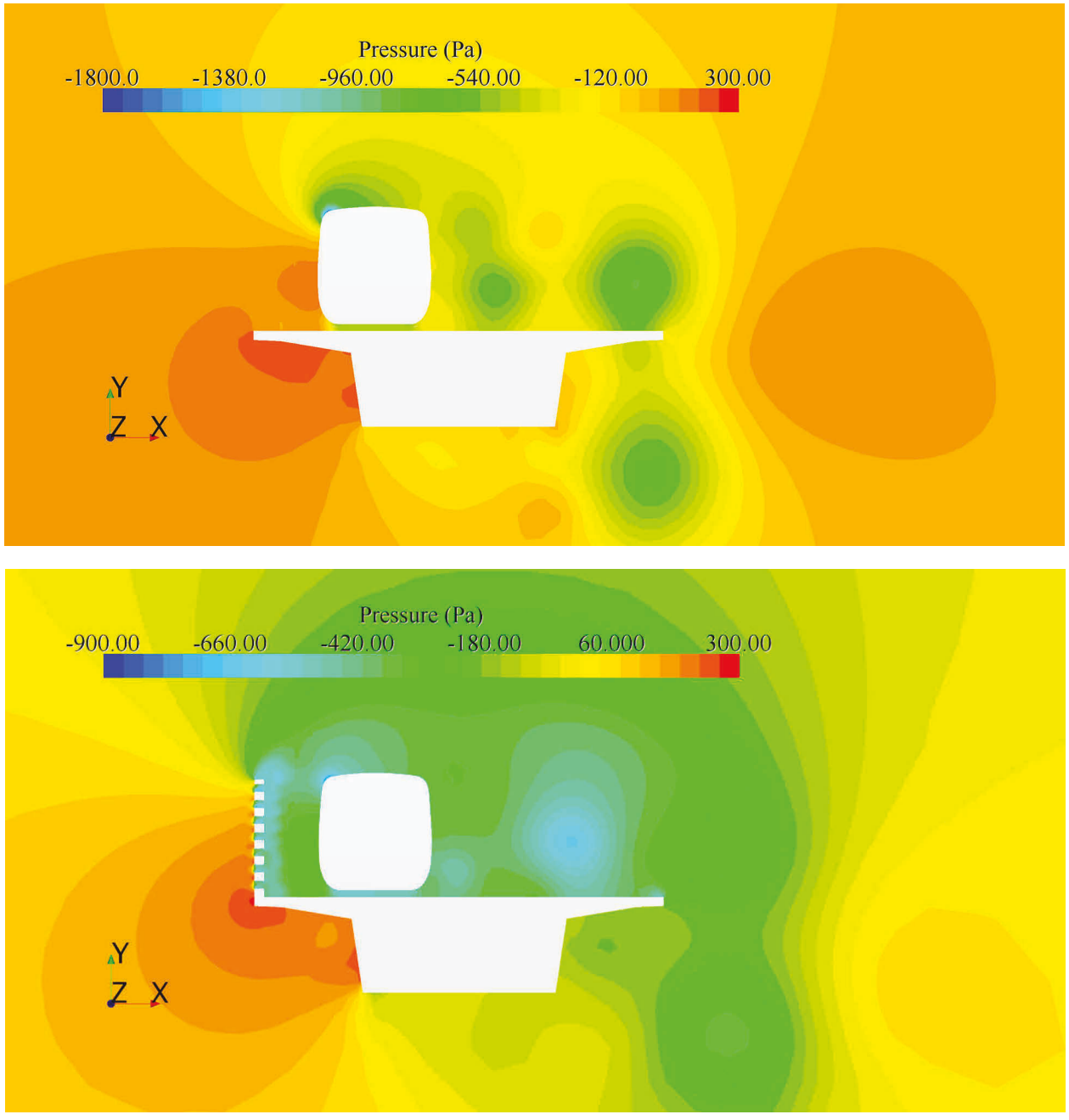

(c)

Figure 7: Pressure contour of the system with no/a wind barrier. (a) Head car. (b) Middle car. (c) Tail car.

Figure 9 denotes the velocity vectors of train-bridge system with no/a wind barrier. It can be seen that there is an obvious eddy domain when the flow passes by the train-bridge system. A big vortex appears obviously behind bridge, and maximum velocity presents on the left corner of the train and bridge evenly. The difference is that when a wind barrier is present, the flow through the barrier creates a large number of small eddies at the gap between the barrier and the train. Without a wind barrier, the maximum wind velocity occurs at the corner of the top and windward sides of the train. After installing the wind barrier, the wind velocity here is significantly reduced.

4.2. Train-Induced Wind Loads. The train aerodynamic force under the effect of train-induced wind is analyzed using the barrier-train-bridge system described in Section 2.3 as the research object.

Figure 10 depicts the temporal histories of vehicle aerodynamic forces. During the driving operation, the train-induced wind generated by the train movement

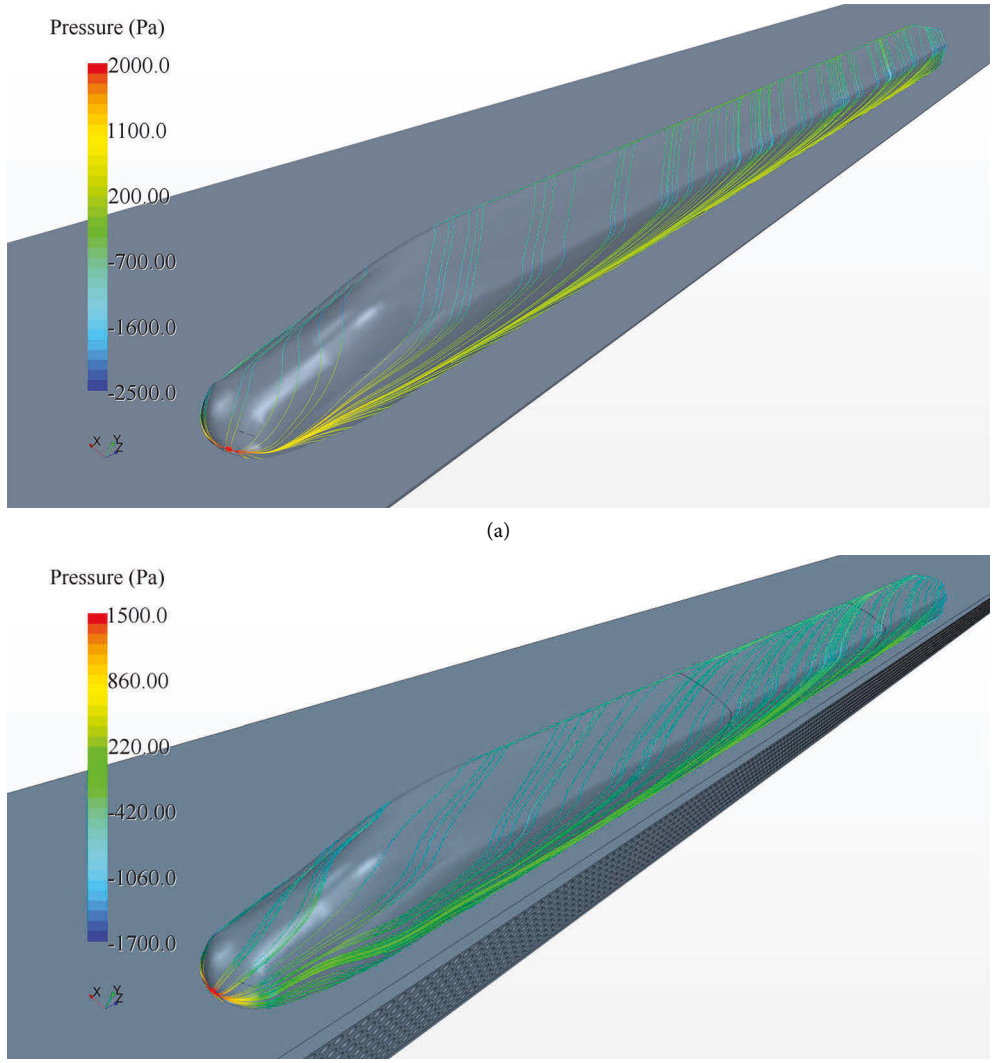

Figure 8: Surface streamlines on the train filed in pressure: (a) with no wind barrier and (b) with a wind barrier.

creates some resistance on the vehicle. The head car is squeezed and the tail car is dragged by the train-induced wind, causing the train to encounter differing resistances in the longitudinal direction. The head vehicle's side force and lift are stronger than the forces in the middle car. This is owing to the distinct directions of crosswind and train-induced wind superimposed on one other. Furthermore, the airflow at the front of the head car is divided, followed by a shift in the airflow structure throughout the train. The findings demonstrate that if the train speed is too high, the head car may be put in danger. The higher the train's speed, the greater the received resistance in the longitudinal direction, which cannot be overlooked. In dynamic response calculations and rail safety evaluations, this must be taken into account.

4.3. Dynamic Response Analysis. A wind barrier-vehicle-bridge system is created and the vibration characteristics are analyzed using the analytical method suggested in Section 2. $U = 20$ m/s and $V = 200$ km/h are the calculation circumstances. The maximal dynamic response of three cars is shown in Table 3. (The car does not distinguish between motor cars and trailers.)

Table 3 shows that, despite the fact that the head and tail cars have essentially the same shape, the effects of train-induced wind on the two cars are distinct, resulting in differing wind loads and dynamic reactions. Except for the unload factor, the head car's three safety indicators and two comfort indications are higher than the tail car's. The middle car's wheelset lateral force, derailment factor, and horizontal and vertical Sperling indices are all in the same range as the head and tail cars. When there is a wind barrier, the train's safety and comfort indices are both lower than its safety limitations. The number of the 6th span's mid-span node when modeling the bridge is B138. B138's acceleration time history curves are shown in Figure 9.

The entire process of vehicles entering the bridge, driving on the bridge, and exiting the bridge is shown in Figure 11.

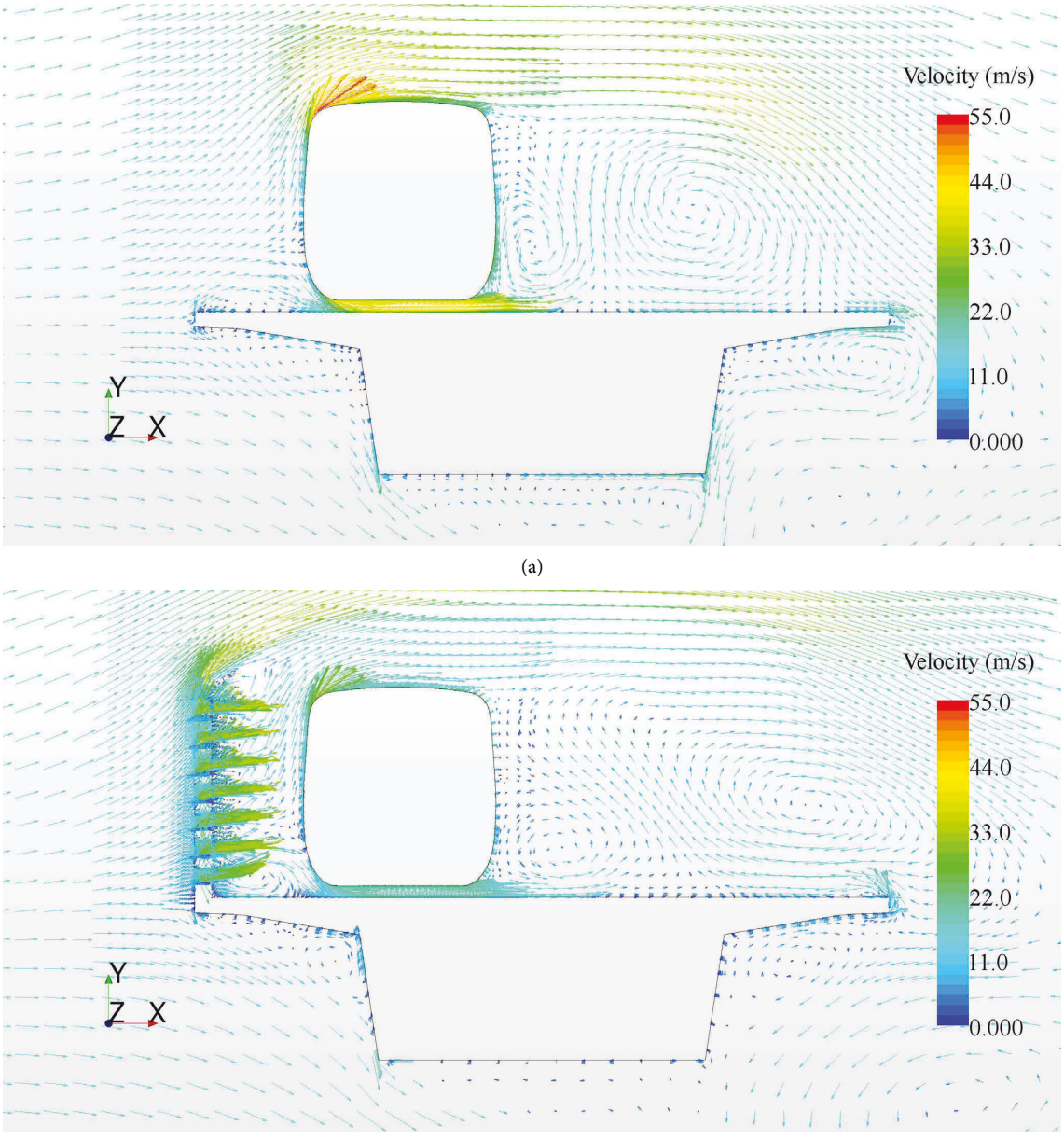

Figure 9: Velocity vectors of train-bridge system: (a) with no wind barrier and (b) with a wind barrier.

The horizontal and vertical acceleration of the bridge both rise when the time is approximately 1 s (the vehicle is on the bridge), owing to the combined impacts of track irregularity, vehicle vibration, and wind load. Node B138 has maximum lateral acceleration of 0.262 m/s^2 and maximum vertical acceleration of 0.624 m/s^2 while traveling at 200 km/h. During the train's departure from the bridge, the acceleration at point B138 steadily decreases to near zero.

4.4. Windbreak Effect and Train-Induced Wind Effect. The dynamic analysis models of the system with or without a wind barrier were compared, and the dynamic responses of the two models were compared under the identical calculation settings, in order to completely analyze the shading impact of the wind barrier and the train-induced wind effect ($U = 20$ m/s; $V = 200$ km/h).

4.4.1. Impact on the Safety of Vehicle Operation. The driving safety indications of vehicles with or without a wind barrier are shown in Figure 12. Figure 12 shows how to compute the windbreak impact on the vehicle safety index, which is the lowering rate of different vehicle safety indices after the wind barrier is built, as shown in Table 4.

The lateral wheel force, derailment factor, offload factor, and overturning factor of the cars were all decreased to varied degrees after the wind barrier was

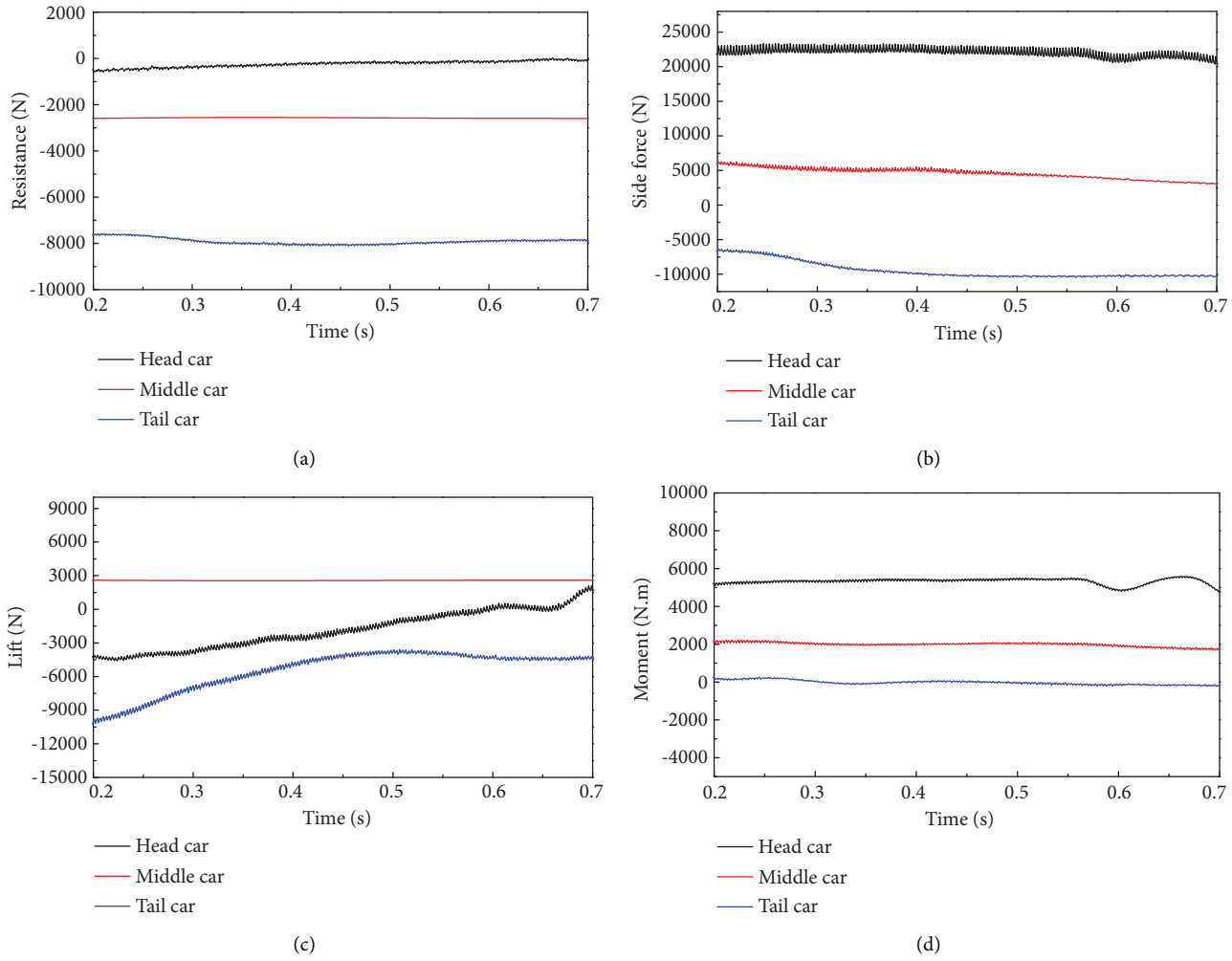

Figure 10: Aerodynamic force curves of each car. (a) Resistance. (b) Side force. (c) Lift. (d) Moment.

Table 3: Maximum dynamic responses of vehicles.

Vehicles	Lateral wheel force (kN)	Derailment factor	Offload factor	Overturning factor	Lateral acc. (m^2/s)	Vertical acc. (m^2/s)	Lateral Sperling	Vertical Sperling
Head car	18.29	0.15	0.20	0.21	0.28	0.35	1.42	1.19
Middle car	16.14	0.15	0.25	0.28	0.33	0.39	1.41	1.19
Tail car	15.02	0.13	0.24	0.12	0.17	0.28	1.23	1.05

installed, as shown in Figure 12 and Table 4. When there is a wind barrier, the head car's lateral wheel force is lowered by 43.5%, and the middle car's lateral wheel force is reduced by almost the same amount, between 24.4% and 30.2%. The head car's derailment factor is lowered by 41.5%, the tail car's is reduced by 1.30%, and the middle car's unload factor is between 24.5 and 33.0%. On the head car, the shielding effect is more noticeable. The offload factors of the head car, middle car, and tail car are all quite close, at 26.6%, 22.4%, and 21.5%, respectively. The overturning factor's law is the same as the unload factor's law. The three autos have almost identical values, and the decrease rate's lowest value is 0.2%. In conclusion, wind barriers lower the quantity of vehicle safety signs while also increasing the safety of operating trains.

4.4.2. Impact on the Comfort of Vehicle Operation. The running stability indicators of vehicles with and without a wind barrier are shown in Figure 13. The horizontal and vertical Sperling indices of the vehicle after installing the wind barrier are less than the constraints and lowered to varied degrees, as shown in Figure 13, and the vertical Sperling index reduction rate is larger than the horizontal Sperling index reduction rate. After the wind barrier is installed, the following happens: ① The lateral Sperling index of the front car is reduced by 1.18%, the lateral Sperling index of the middle car is reduced by 1.04%–6.3%, and the lateral Sperling index of the tail car is reduced by 5.52%. ② The vertical Sperling index of the head car is reduced by 35.4% and the tail car by 36.3%, and the vertical Sperling reduction rate of the middle car is basically the

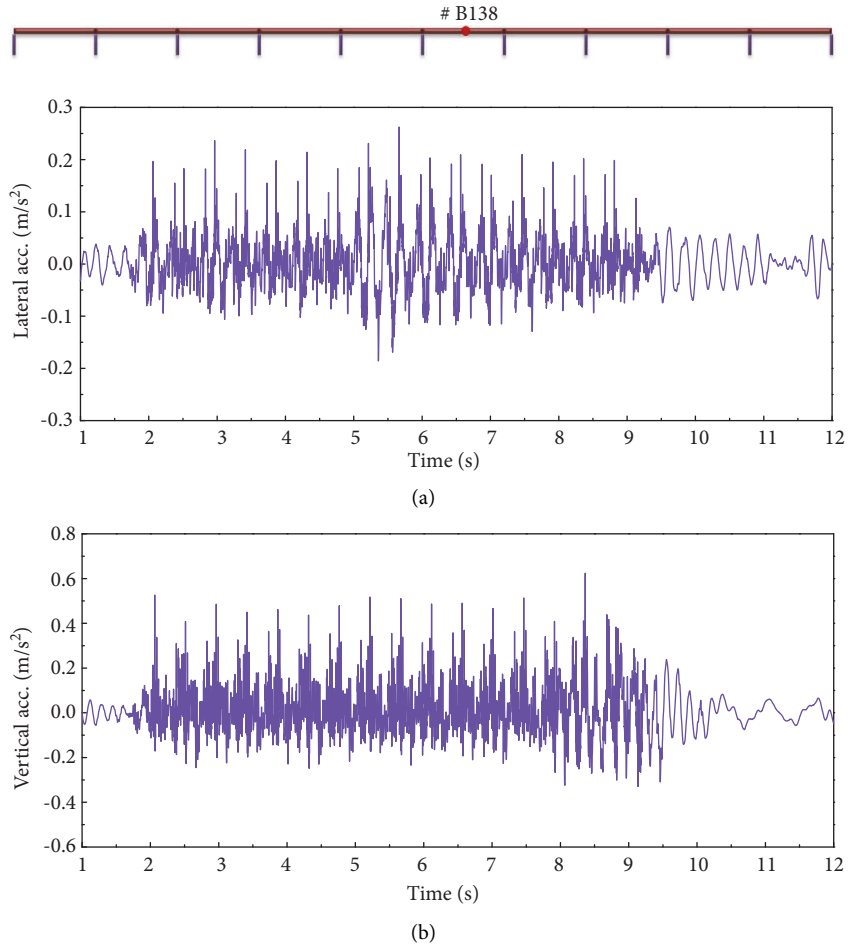

Figure 11: Acceleration time histories of node B138. (a) Lateral acceleration. (b) Vertical acceleration.

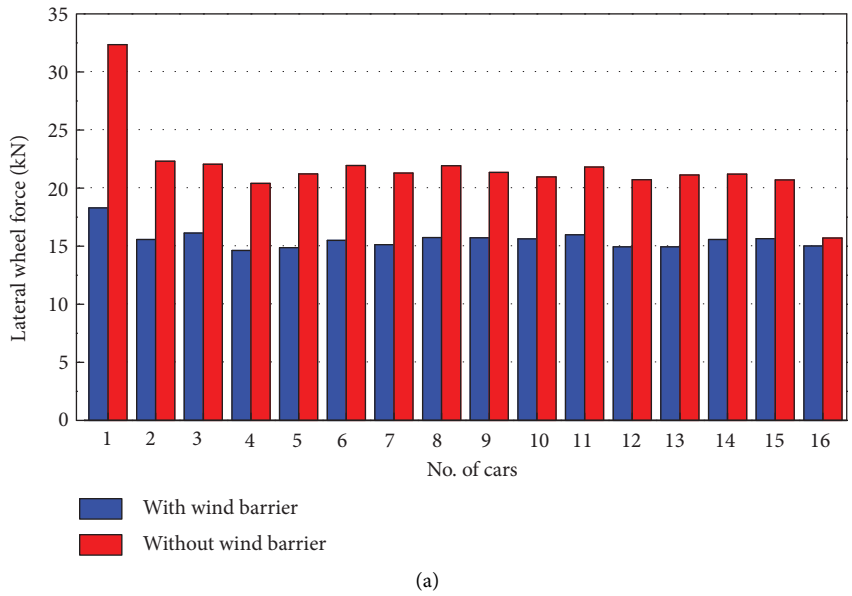

Figure 12: Continued.

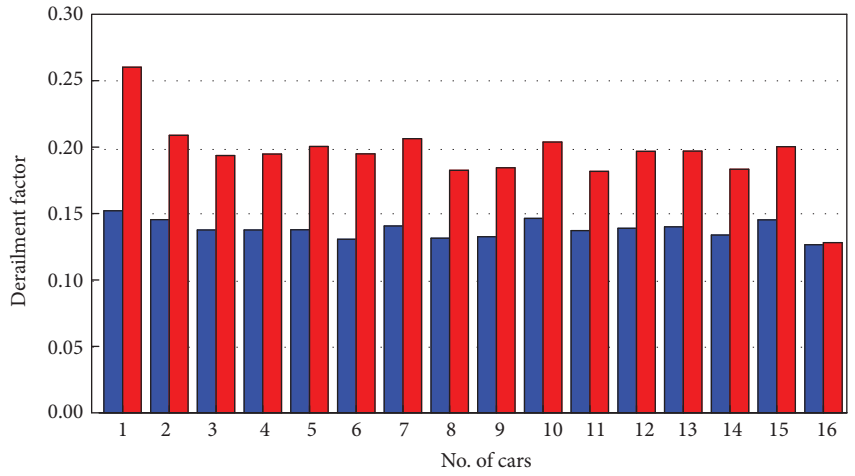

(b)

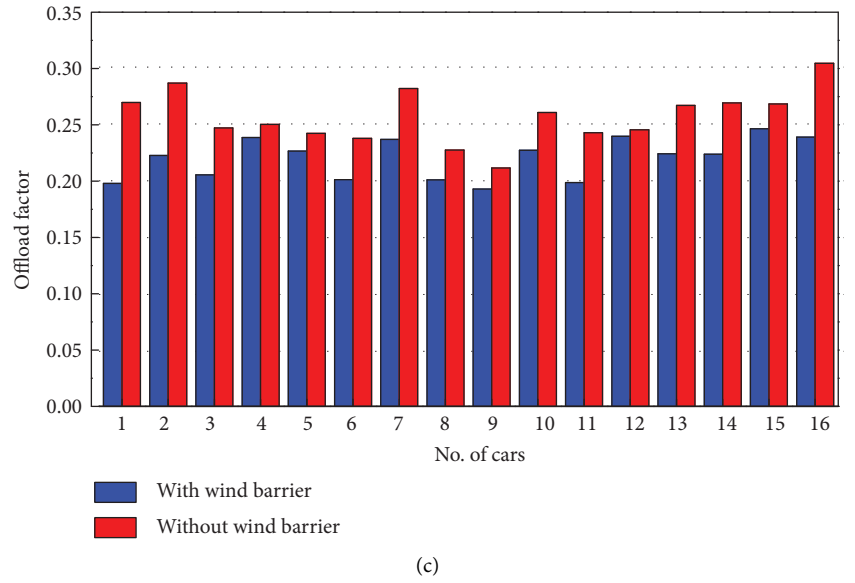

(c)

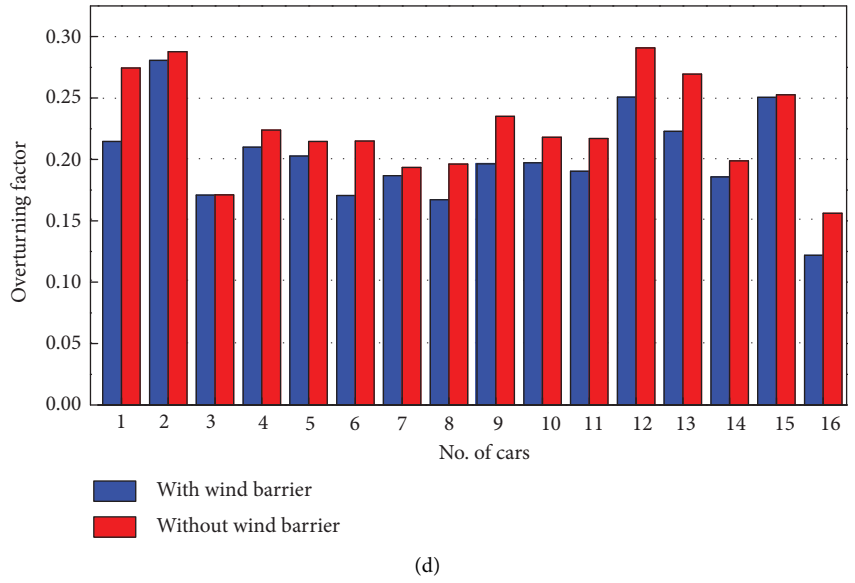

(d)

Figure 12: Running safety indices of vehicles with/without wind barrier. (a) Lateral wheel force. (b) Derailment factor. (c) Offload factor. (d) Overturning factor.

Table 4: Windbreak effect of wind barrier.

Vehicles	Lateral wheel force	Derailment factor	Offload factor	Overturning factor
Head car (%)	43.5	41.5	26.6	21.8
Middle car (%)	30.2	33.0	22.4	20.6
Tail car (%)	4.30	1.30	21.5	21.9

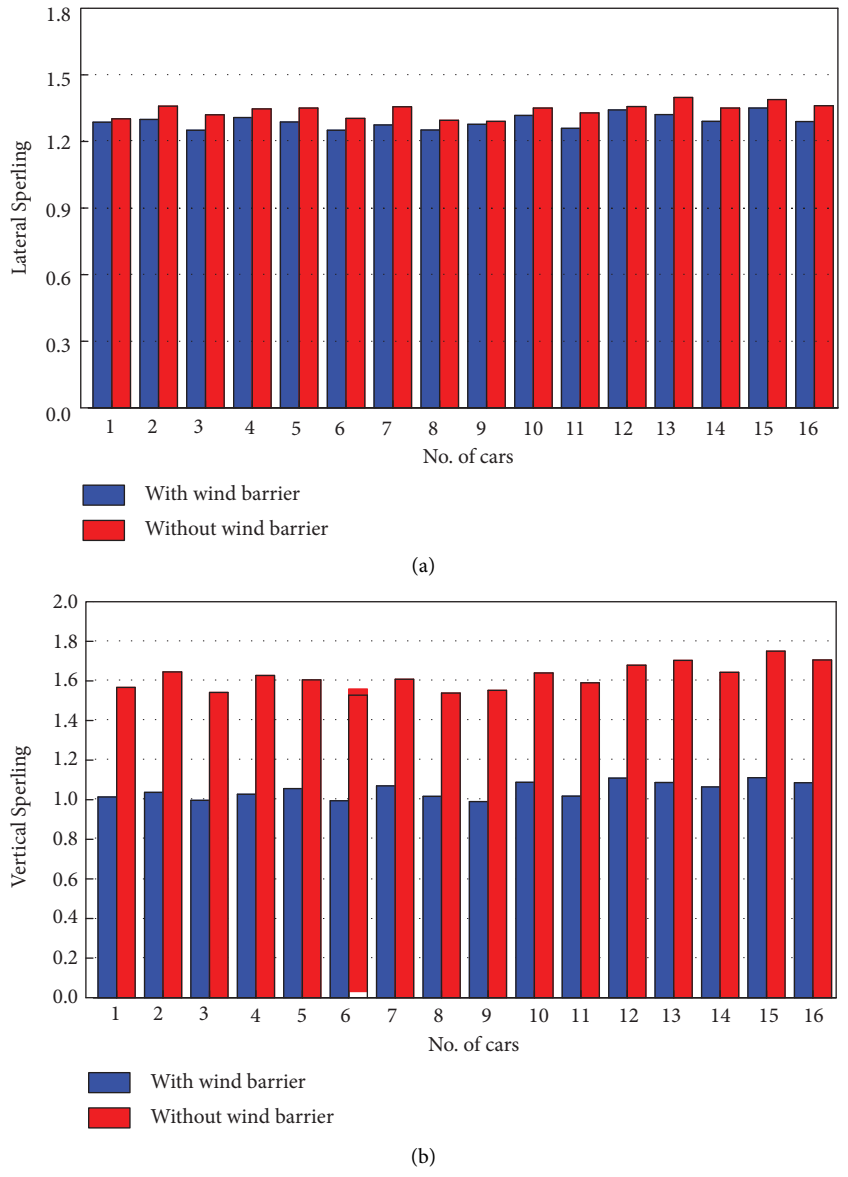

Figure 13: Running stability indices of vehicles with/without wind barrier. (a) Lateral Sperling. (b) Vertical Sperling.

same. The wind barrier may considerably lower the vehicle's vertical comfort index and boost passenger comfort, which is favorable to the train's operation.

4.4.3. Impact on Bridge Dynamic Responses. Figures 14 and 15 show the acceleration and displacement time histories of node B138 with or without a wind barrier.

Figure 14 shows that after the wind barrier was installed, the maximum lateral acceleration of the bridge's node B138 rose by 10.08%, from 0.238 m/s^2 to 0.262 m/s^2. The maximum vertical acceleration increased by 8.15% from 0.577 m/s^2 to 0.624 m/s^2.

Figure 15 shows that after installing the wind barrier, the maximum lateral displacement of node 138 increased by 43.6%, from 0.522 mm to 0.750 mm. Because of the wind barrier, the bridge's geometry and aerodynamic form altered, affecting the wind field of the whole system and reducing vertical displacement marginally. Because the vehicle

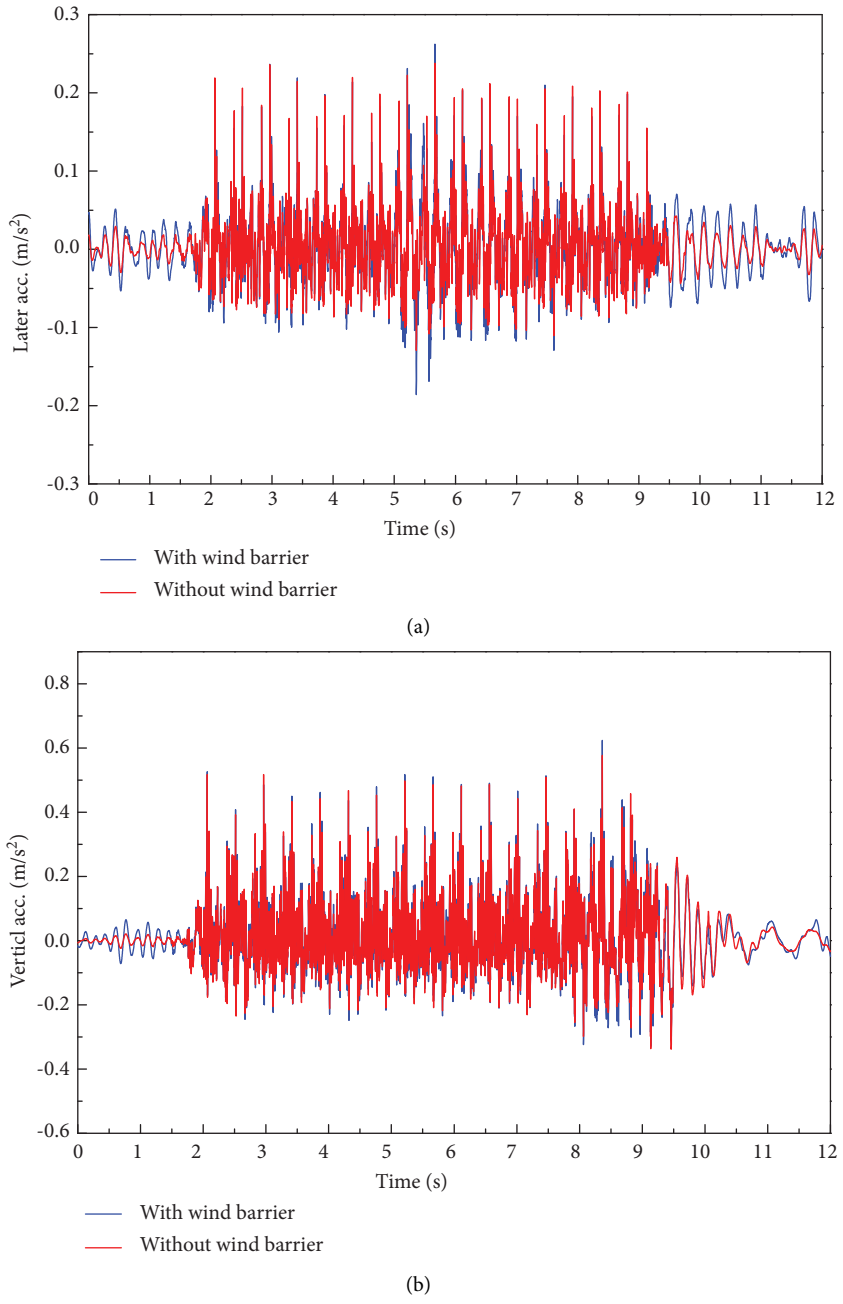

Figure 14: Acceleration time histories of node B138 with/without wind barrier. (a) Lateral acceleration. (b) Vertical acceleration.

is the primary load operating on the bridge in the vertical direction, the vertical displacement of the bridge is mostly determined by the gravity of the wheelset. In conclusion, the wind barrier increases the bridge's acceleration response and lateral displacement, which is to some degree detrimental to the bridge.

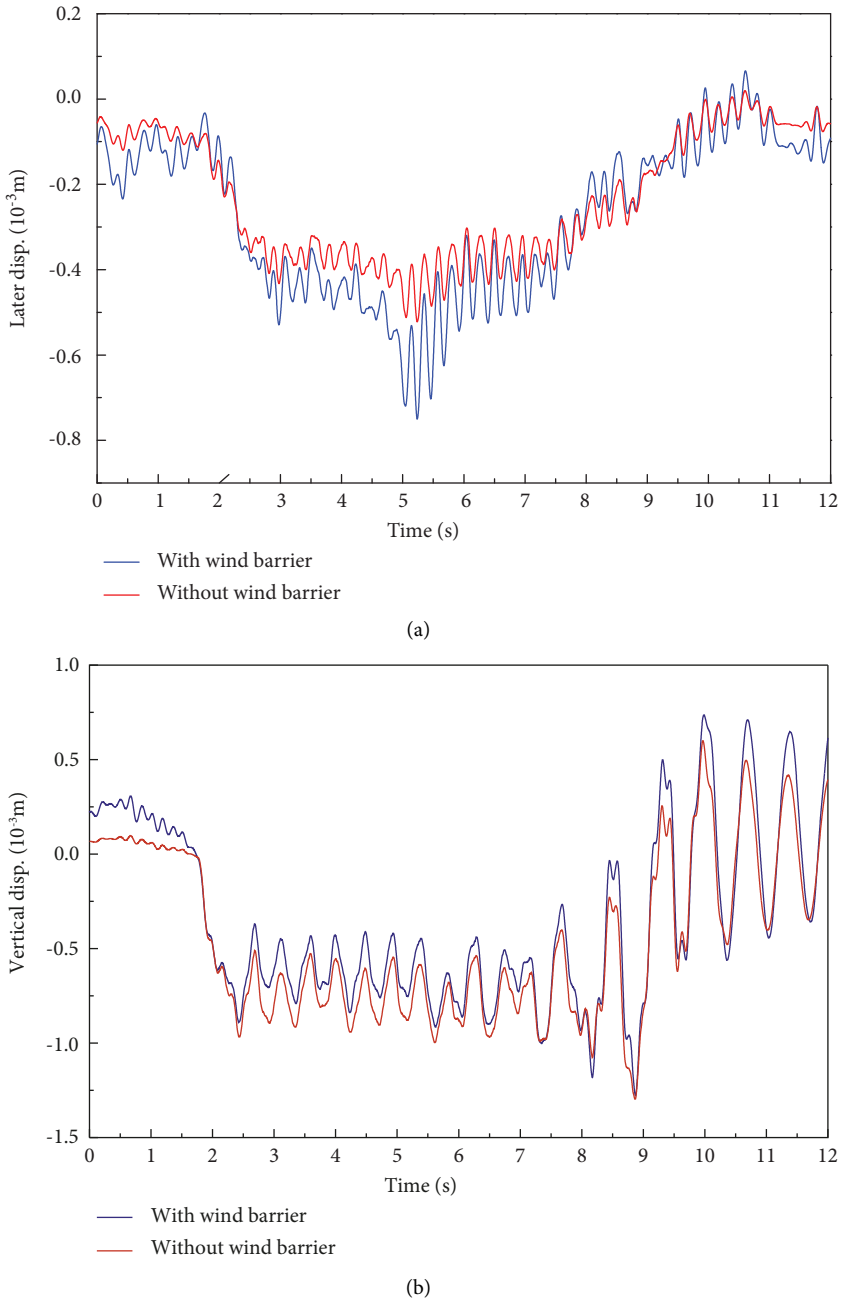

Figure 15: Displacement time histories of node B138 with/without wind barrier. (a) Lateral displacement. (b) Vertical displacement.

5. Conclusions

The wind load of the train and bridge is calculated using a numerical simulation method in this paper, which takes into account the wind shielding effect of the wind barrier as well as the train-induced wind effect of the train. The effect of the wind barrier on the train's safety and the bridge's dynamic reaction is studied. The following are some of the conclusions:

(1) The train forms a particular angle with the combined wind field generated by the superposition of the crosswind perpendicular to the train's running direction and the train-induced wind along the train's running direction. Although the shapes of the head car and the tail car are similar, due to the train-induced wind effect, their loads are different, so the dynamic responses of the two are also different.

(2) Due to the presence of holes, the vortex between the wind barrier and the train's windward surface changes in a very complicated way. The airflow traveling through the perforations has a negative value because it circulates at the intersection of the windward surface and the top surface of the car body.

(3) The maximum values of lateral wheel force, derailment factor, offload factor, and overturning factor of

the vehicle are reduced by 43.5%, 42.3%, 26.6%, and 21.9%, respectively, when a wind barrier is present, which is conducive to driving. The shielding effect of the wind barrier on the head vehicle is more visible in terms of wheel lateral force and derailment factor.

(4) The horizontal and vertical acceleration and the lateral displacement of the bridge's mid-span node increased by 10.08%, 8.15%, and 43.6%, respectively, in the case of a wind barrier. To some degree, the wind barrier is harmful to the bridge. In addition, when the wind barrier is erected, the wind field surrounding the bridge becomes exceedingly convoluted, resulting in a minor decrease in vertical displacement.

This paper primarily proposes a vehicle-bridge coupled dynamic calculation approach that takes into account both the train-induced wind and the wind barrier's wind shielding effect. On the basis of the old technique, this method modifies the calculating method for railway and bridge wind loads. The numerical simulation approach is used to analyze the train-induced wind effect while the train is running at the actual speed, which is distinct from the usual calculation method. The authors used STAR-CCM+, Ansys software, and MATLAB self-programming for all calculations. With the arrival of the high-speed rail era, train speeds will reach 400 km/h, necessitating a greater focus on the train's wind impact. The parameter analysis of wind velocity, vehicle speed, and wind attack angle is not carried out in this paper due to the large burden of wind load calculation. These factors will be used in future study to better examine train safety and give a theoretical foundation for the speed increase of high-speed trains.

Data Availability

The data used to support the findings of this study are available from the corresponding author upon request.

Conflicts of Interest

The authors declare that they have no conflicts of interest.

Acknowledgments

The authors are grateful to the Doctoral Fund Project (X20024Z), the Shandong Provincial Natural Fund Project (ZR2021ME104), and the Science and Technology Project of Shandong Provincial Department of Transportation (2020B69).

References

[1] J. W. Chen, G. J. Gao, and C. L. Zhu, "Detached-eddy simulation of flow around high-speed train on a bridge under cross winds," *Journal of Central South University*, vol. 23, no. 10, pp. 2735–2746, 2016.

[2] X. He, K. Shi, T. Wu, and Y. Zou, "Aerodynamic performance of a novel wind barrier for train-bridge system," *Wind and Structures*, vol. 23, no. 3, pp. 2–20, 2016.

[3] Y. Dai, X. Dai, Y. Bai, and X. He, "Aerodynamic performance of an adaptive GFRP wind barrier structure for railway bridges," *Materials*, vol. 13, no. 18, p. 4214, 2020.

[4] M. Mohebbi and M. A. Rezvani, "Analysis of the effects of lateral wind on a high speed train on a double routed railway track with porous shelters," *Journal of Wind Engineering and Industrial Aerodynamics*, vol. 184, pp. 116–127, 2019.

[5] P. A. Montenegro, R. Calada, H. Carvalho, and A. Bolkovoy, "Stability of a train running over the Volga river high-speed railway bridge during crosswinds," *Structure & Infrastructure Engineering*, vol. 16, no. 8, pp. 1121–1137, 2020.

[6] Y. Wang, H. Xia, W. Guo, and N. Zhang, "Numerical analysis of wind field induced by moving train on HSR bridge subjected to crosswind," *Wind and Structures*, vol. 27, no. 1, pp. 29–40, 2018.

[7] H. X. Hui, D. X. Fang, L. I. Huan, and K. Shi, "Parameter optimization for improved aerodynamic performance of louver-type wind barrier for train-bridge system," *Journal of Central South University*, vol. 26, no. 1, pp. 229–240, 2019.

[8] X. H. Xiong, B. Yang, K. W. Wang, T. H. Liu, Z. He, and L. Zhu, "Full-scale experiment of transient aerodynamic pressures acting on a bridge noise barrier induced by the passage of high-speed trains operating at 380–420 km/h," *Journal of Wind Engineering and Industrial Aerodynamics*, vol. 204, Article ID 104298, 2020.

[9] C. Luo, D. Zhou, G. Chen, S. Krajnovic, and J. Sheridan, "Aerodynamic effects as a maglev train passes through a noise barrier," *Flow, Turbulence and Combustion*, vol. 105, no. 3, pp. 761–785, 2020.

[10] H. Gu, T. Liu, and Z. Jiang, "Research on the wind-sheltering performance of different forms of corrugated wind barriers on railway bridges," *Journal of Wind Engineering and Industrial Aerodynamics*, vol. 201, Article ID 104166, 2020.

[11] A. Buljac, H. Kozmar, S. Posplsil, M. Machacek, and S. Kuznetsov, "Effects of wind-barrier layout and wind turbulence on aerodynamic stability of cable-supported bridges," *Journal of Bridge Engineering*, vol. 25, no. 12, Article ID 04020102, 2020.

[12] E. Deng, W. Yang, X. He et al., "Aerodynamic response of high-speed trains under crosswind in a bridge-tunnel section with or without a wind barrier," *Journal of Wind Engineering and Industrial Aerodynamics*, vol. 210, no. 1, Article ID 104502, 2021.

[13] E. Deng, W. Yang, L. Deng, Z. Zhu, X. He, and A. Wang, "Time-resolved aerodynamic loads on high-speed trains during running on a tunnel–bridge–tunnel infrastructure under crosswind," *Engineering Applications of Computational Fluid Mechanics*, vol. 14, no. 1, pp. 202–221, 2020.

[14] S. Huang, H. Hemida, and M. Z. Yang, "Numerical calculation of the slipstream generated by a CRH2 high-speed train," *Proceedings of the Institution of Mechanical Engineers - Part F: Journal of Rail and Rapid Transit*, vol. 230, no. 1, pp. 103–116, 2016.

[15] H. Hemida, C. Baker, and G. Gao, "The calculation of train slipstreams using large-eddy simulation," *Proceedings of the Institution of Mechanical Engineers - Part F: Journal of Rail and Rapid Transit*, vol. 228, no. 1, pp. 25–36, 2014.

[16] F. Dorigatti, M. Sterling, C. J. Baker, and A. Quinn, "Crosswind effects on the stability of a model passenger train—a comparison of static and moving experiments," *Journal of Wind Engineering and Industrial Aerodynamics*, vol. 138, no. 0, pp. 36–51, 2015.

[17] H. Xiang, Y. Li, S. Chen, and C. Li, "A wind tunnel test method on aerodynamic characteristics of moving vehicles under

crosswinds," *Journal of Wind Engineering and Industrial Aerodynamics*, vol. 163, pp. 15–23, 2017.

[18] Y. L. Li, H. Y. Xiang, B. Wang, Y. L. Xu, and S. Z. Qiang, "Dynamic analysis of wind-vehicle-bridge coupling system during the meeting of two trains," *Advances in Structural Engineering*, vol. 16, no. 10, pp. 1663–1670, 2013.

[19] Y. Bao, W. Zhai, C. Cai, S. Zhu, and Y. Li, "Dynamic interaction analysis of suspended monorail vehicle and bridge subject to crosswinds," *Mechanical Systems and Signal Processing*, vol. 156, no. 2, Article ID 107707, 2021.

[20] T. Zhang, H. Xia, and W. W. Guo, "Analysis on running safety of train on bridge with wind barriers subjected to cross wind," *Wind and Structures An International Journal*, vol. 17, no. 2, 2013.

[21] T. Zhang, H. Xia, and W. W. Guo, "Analysis on running safety of train on the bridge considering sudden change of wind load caused by wind barriers," *Frontiers of Structural & Civil Engineering*, vol. 12, no. 4, pp. 558–567, 2018.

[22] W. Guo, Y. Wang, H. Xia, and S. Lu, "Wind tunnel test on aerodynamic effect of wind barriers on train-bridge system," *Science China Technological Sciences*, vol. 58, no. 2, pp. 219–225, 2015.

[23] Y. Cao, H. Xiang, and Y. Zhou, "Simulation of stochastic wind velocity field on long-span bridges," *Journal of Engineering Mechanics*, vol. 126, no. 1, pp. l–6, 2000.

[24] H. Xia, N. Zhang, and W. Guo, *Dynamic Interaction of Train-Bridge Systems in High-Speed Railways: Theory and Applications*, Beijing Jiaotong University Press, Beijing, 2018.

[25] N. Zhang and H. Xia, "Dynamic analysis of coupled vehicle–bridge system based on inter-system iteration method," *Computers & Structures*, vol. 114-115, pp. 26–34, 2013.